VLT observations of the asymmetric Etched Hourglass Nebula, MyCn 18

N. Clyne[1], M.P. Redman[1], M. Lloyd[2], M. Matsuura[3], N. Singh[1], J. Meaburn[2]

[1] Centre for Astronomy, School of Physics, National University of Ireland Galway, University Road, Galway, Ireland
   e-mail: n.clyne1@nuigalway.ie, matt.redman@nuigalway.ie

[2] Jodrell Bank Centre for Astrophysics, School of Physics and Astronomy, University of Manchester, Oxford Road, Manchester M13 9PL, UK

[3] Department of Physics and Astronomy, University College London, Gower Street, London WC1E 6BT, UK

August 19, 2014

ABSTRACT

Context. The mechanisms that form extreme bipolar planetary nebulae remain unclear.

Aims. The physical properties, structure, and dynamics of the bipolar planetary nebula, MyCn 18, are investigated in detail with the aim of understanding the shaping mechanism and evolutionary history of this object.

Methods. VLT infrared images, VLT ISAAC infrared spectra, and long-slit optical Echelle spectra are used to investigate MyCn 18. Morpho-kinematic modelling was used to firmly constrain the structure and kinematics of the source. A timescale analysis was used to determine the kinematical age of the nebula and its main components.

Results. A spectroscopic study of MyCn 18's central and offset region reveals the detailed make-up of its nebular composition. Molecular hydrogen, atomic helium, and Bracket gamma emission are detected from the central regions of MyCn 18. ISAAC spectra from a slit position along the narrow waist of the nebula demonstrate that the ionised gas resides closer to the centre of the nebula than the molecular emission. A final reconstructed 3-D model of MyCn 18 was generated, which provides kinematical information on the expansion velocity of its nebular components by means of position-velocity (P-V) arrays. A kinematical age of the nebula and its components were obtained by the P-V arrays and timescale analysis.

Conclusions. The structure and kinematics of MyCn 18 are better understood using an interactive 3-D modelling tool called SHAPE. A dimensional and timescale analysis of MyCn 18's major components provides a possible mechanism for the nebula's asymmetry. The putative central star is somewhat offset from the geometric centre of the nebula, which is thought to be the result of a binary system. We speculate that the engulfing and destruction of an exoplanet during the AGB phase may have been a key event in shaping MyCn 18 and generating of its hypersonic knotty outflow.

Key words. Planetary nebulae: individual: MyCn 18 – Stars: binaries: general – Stars: kinematics and dynamics – Stars: winds, outflows – Stars: circumstellar matter – Infrared: general

1. Introduction

MyCn 18 (RA=13h39m35.07s, Dec=−67d22m51.7s (J2000); PN G307.5−04.9; IRAS 13359−6707) is a beautiful example of an extremely tightly waisted bipolar planetary nebula (PN). The famous HST images of Sahai et al. (1999), who christened it the Etched Hourglass Nebula, show the remarkable degree of symmetry in the nebula and also the clear offset of the central star along the nebular minor axis. The question of how the diverse range of PNe shapes are produced from what is presumably a spherical AGB star (Soker & Harpaz 1992; Trammell et al. 1995; Sahai & Trauger 1998; Sahai et al. 2009) continues to intrigue astronomers and the extreme case of MyCn 18 provides a stern test of any evolutionary model.

The tight-waisted appearance of MyCn 18 led Corradi & Schwarz (1993) to compare it to two apparently similar symbiotic nebulae He2-104 and BI Cru. However, they concluded that, other than the striking morphological similarity, there was no other evidence pointing to MyCn 18 being a post-PN symbiotic nebula and that it should tentatively be classed as a young PN, on the basis of its position in optical and near-IR diagnostic diagrams.

Bryce et al. (1997) discovered hypersonic (~500 km s^{-1}) knots situated on either side of the main hourglass nebula, approximately along the polar axis. It is interesting to note that these knots are travelling much faster than the expansion velocity of the hourglass shell (~50 km s^{-1}). Such speeds are similar to those found by Corradi & Schwarz (1993) for the symbiotic nebulae He2-104 and BI Cru. O'Connor et al. (2000) demonstrated that the knots of MyCn 18 had a degree of point symmetry and that the radial speed of each knot increased linearly with its distance from the central star. They speculated that MyCn 18 might be morphologically related to the symbiotic nebulae.

The HST images of Sahai et al. (1999) revealed a wealth of structural detail in the main nebula, which appears to contain a second, inner, hourglass-shaped structure, as well as two central rings. Each of these structures has a slightly different geometric centre, none of which are coincident with the central star. Dayal et al. (2000) showed that the nebula is generally density-bounded except in the region of the hourglass waist. They also inferred that the etched arcs on the hourglass walls might indicate temporal variations in the mass-loss rate of the progenitor star. Bains et al. (2002) found a similar geometric offset between the nebula and the central star when observing at radio wavelengths. Their spectral index maps show that the nebular core
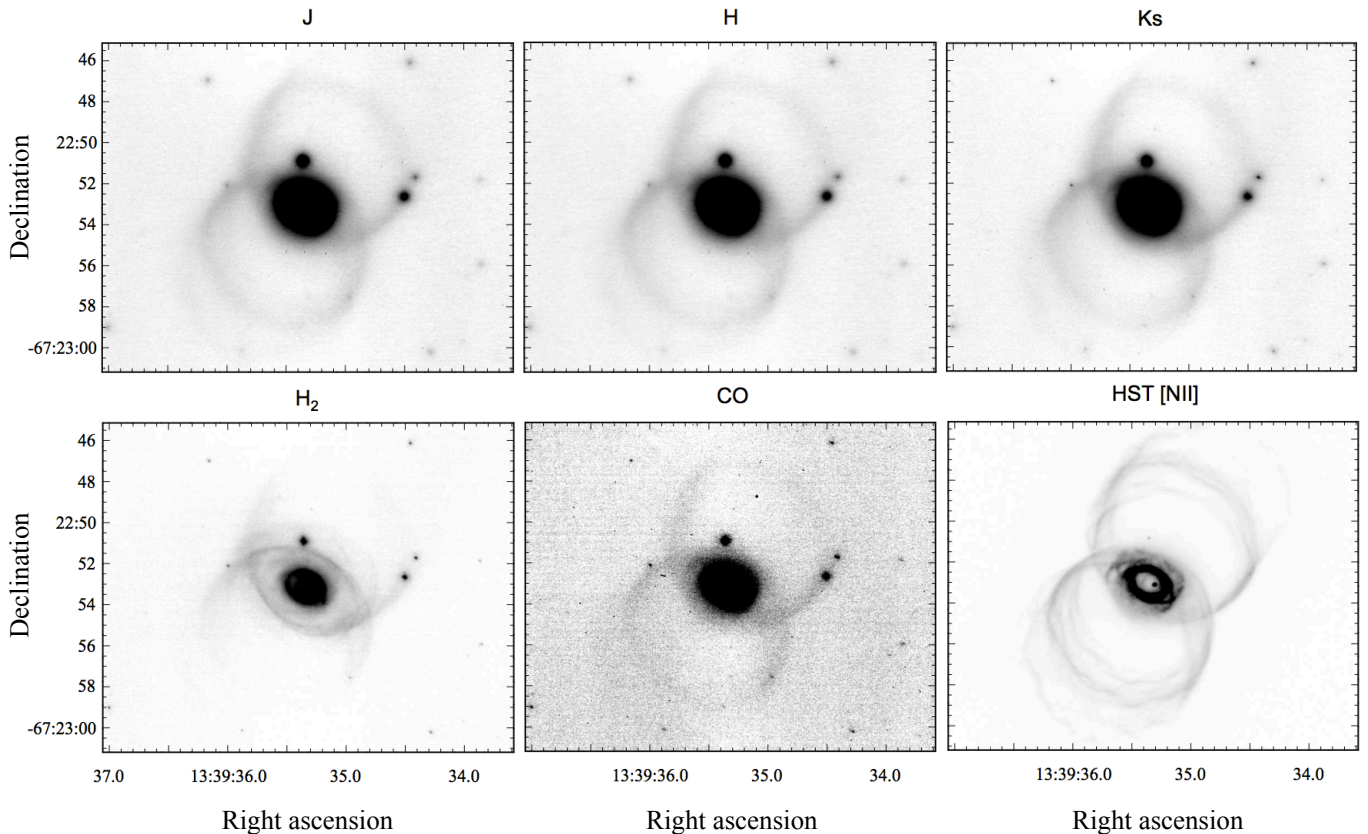
Fig. 1. Images of the bulk of MyCn 18's nebulosity. Presented are a series of linear greyscale infra-red images obtained using the J, H, and Ks broadband filters, along with H_2 and CO images using the NB_2.12 and IB_2.30 filters, respectively. An archival HST [N II]6584 Å linear greyscale image is also included to compare and display the nebula's more distinct features.

appears to be more optically thick than the lobe regions at lower frequencies (1384 and 4800 MHz). The relatively low brightness temperatures were interpreted as a result of beam dilution of a clumpy structure inferred a filling factor of 0.15 at 1384 MHz. Their estimated total ionised mass of the nebula is in the region 0.2–0.8 $M_\odot$ at a distance of 2.4 kpc.

Whitelock (1985) presented JHK photometry for a sample of southern PNe and showed that the major source of the near-IR radiation from MyCn 18 is nebular in origin. Molecular hydrogen has been detected in many PNe (Hora & Latter 1996; Kastner et al. 1998; Likkel et al. 2000; Kastner et al. 2000; Davis et al. 2003; Aleman & Gruenwald 2004; Eyermann & Speck 2004; Matsuura & Zijlstra 2005; Hora et al. 2005; Wang et al. 2006; Matsuura et al. 2007; Sellgren et al. 2008; Ramos-Larios et al. 2008; Tenenbaum et al. 2009), and given that MyCn 18 is believed to be ionisation-bounded at its waist, it is likely that any available molecular hydrogen will be found around this region. Sahai et al. (1999) pointed out that the expected K-band photospheric flux (derived from optical photometry) is about half of the observed value, indicating that the central star is probably surrounded by hot dust in the waist region.

The hourglass shape of MyCn 18 is possibly formed by a fast, tenuous wind expanding within a more slowly expanding cloud, which has a higher density near its equatorial region than near its polar regions. This snow-plow-like process was first introduced by Kwok et al. (1978), as the interacting stellar winds (ISW) theory of nebular formation, and later as the generalised interacting stellar winds (GISW) model (Kwok 1982; Balick

1987). The HST images of MyCn 18 reveal both intricate patterns (etchings) along its nebular walls and weak emission with filamentary components just beyond the walls. MyCn 18 is a good example of an extreme bipolar PN with strong asymmetry or axi-symmetry. This bipolar shape might also be the result of the formation of a dense equatorial accretion/excretion disk or of high-velocity collimated outflows, as discussed by Sahai et al. (1999).

The mechanism for generating extreme deviations from spherical symmetry in planetary nebulae remains unsettled. Models and explanations range from single stars with particular magnetic fields arrangements (Chevalier & Luo 1994; García-Segura et al. 1999; Pascoli & Lahoche 2008; Vlemmings 2011; Jordan et al. 2012; Vlemmings 2012) to the view that almost all planetary nebulae are caused by binary companions (Yungelson et al. 1993; Soker & Rappaport 2001; De Marco 2009; Jones et al. 2010; Douchin et al. 2012; Jones et al. 2012). The discovery that hot Jupiter exoplanets are common around stars means that large planetary mass companions can also be considered amongst the shaping mechanisms (Nordhaus & Blackman 2006). Clearly it is of interest to search for a binary star in MyCn 18. The identification of the central ionising star in MyCn 18 appears quite firm though it is clearly noticeable that the star is significantly offset from the geometrical centre of the outer and inner hourglass, as identified by Sahai et al. (1999).

In order to further our understanding of this striking nebula we have carried out an infra-red and spectroscopic study of
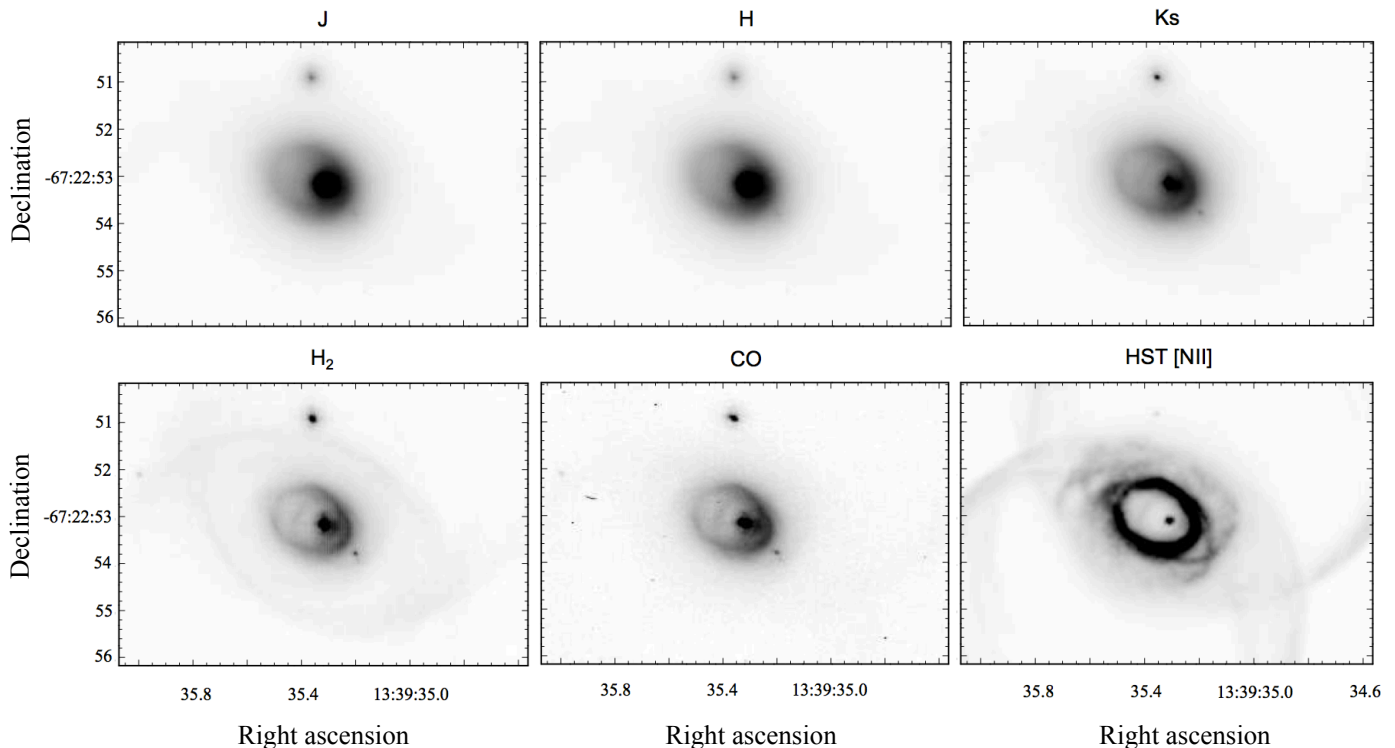
Fig. 2. Linear stretches of the images in Fig. 1. The central region of each image is displayed at a higher contrast linear scale to show the features of interest not apparent in Fig. 1. The stretches, in comparison to those images in Fig. 1, are as follows: x10 for J, H, Ks and CO, x4 for H_2, and x2 for [N II]6584 Å.

MyCn 18 and used a 3-D morpho-kinematic code called SHAPE[1] (Steffen et al. 2011) to carefully reproduce the structural and spectral features of the nebula.

The paper is organised as follows: The observational data are presented in Sect. 2. Analyses of each topic are presented in Sect. 3. This section includes: infra-red imaging, spectroscopic analysis, the modelling of optical kinematic data using SHAPE, a geometric dimensional analysis of the outer and inner regions of the nebula, and a timescale analysis of the nebula's three major components. A discussion and conclusions are found in Sect. 4 and Sect. 5, respectively.

2. Observations and results

2.1. Infra-red images

A series of infra-red images of MyCn 18 were obtained in photometric conditions on 27 May 2003 using NAOS-CONICA (NACO: Rousset et al. 2003; Lenzen et al. 2003) on ESO's VLT(UT4) telescope. NACO was used with the S27 camera (0.027 arcsec per pixel and a field of view of 28 × 28 arcsec).

Continuum images were obtained using the J, H, and Ks broadband filters. The NB_2.12 filter was used to image the H_2 (1-0) S(1) emission line and the IB_2.30 filter was used to look for evidence of CO 2.295 μm emission. The filters, exposure times, and image resolution are detailed in Table 1.

The central star of MyCn 18 [m_v = 14.9 and spectral type Of(C); as noted by Sahai et al. (1999) and Lee et al. (2007), respectively] was used as the AO reference star, with optical wavefront sensing via the VIS dichroic. Optical

---

[1] SHAPE is accessible online at http://www.astrosen.unam.mx/shape/

Table 1. Filters used for the NACO observations

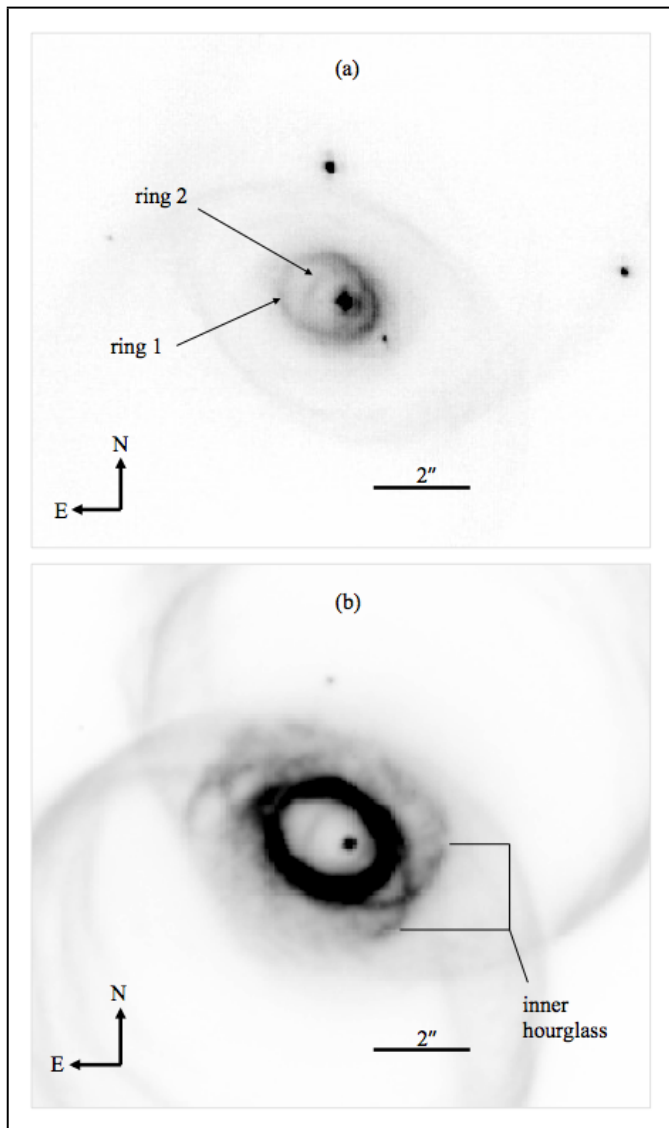| Filter	λ_c (μm)	$\Delta\lambda$ (μm)	t_{exp} (s)	Resolution
J	1.265	0.25	1100	0.20″ × 0.19″
H	1.66	0.33	1100	0.18″ × 0.11″
Ks	2.18	0.35	1600	0.13″ × 0.11″
NB_2.122	2.122	0.022	3720	0.11″ × 0.09″
IB_2.30	2.30	0.06	540	0.13″ × 0.09″

Notes. A list of the filters used for the NACO observations, giving the λ_c and $\Delta\lambda$ for each filter together with the total on-target integration time and the resolution as measured from the psf of the star to the northeast of the nebular core.

seeing at the observatory was 0.4–1.1 arcsec FWHM during the observed period. The observations were taken with the NACO_img_obs_FixedSkyOffset template using a 4 arcsec square jitter box and sky offset position 35 arcsec to the NE of the target position.

The data were reduced using a tailored version of the ORAC-DR pipeline (Cavanagh et al. 2008) invoking the UKIRT imaging recipes (Currie & Cavanagh 2004), which had been adapted to account for NACO's tiny point-spread function. The final image from each filter was then aligned with the Ks image. These images are shown in Fig. 1, along with the narrowband [N II]6584 Å HST image (Sahai et al. 1999), which has been regridded to the NACO pixel scale and aligned with the Ks image for consistency (The resolution of this image is about 0.09 × 0.09 arcsec). Note that neither the H_2 nor the CO images have been continuum subtracted. The NB_2.122 filter, used

for the H_2 observations, produces a very irregular point spread function, and due to this irregularity we were unable to create a satisfactory continuum subtracted image. The stretch levels used for all images in both Fig. 1 and 2 are tabulated in Table 2.

Table 2. Linear greyscale cut off levels used in Figs. 1 and 2

Fig	J	H	Ks	H_2	CO	N II
1	0–20	0–20	0–16	0–15	0–10	0–800
2	0–200	0–200	0–160	0–60	0–100	0–1600

Notes. Scaling was chosen to highlight the nebular features. The scales are in counts but are not flux calibrated. Individual frame exposure times were 10 s for J, H, and Ks, and 60 s for CO and H_2. The images shown in both figures are the combined and reduced images for each filter but with counts averaged to the exposure time for one image to give a better signal-to-noise.
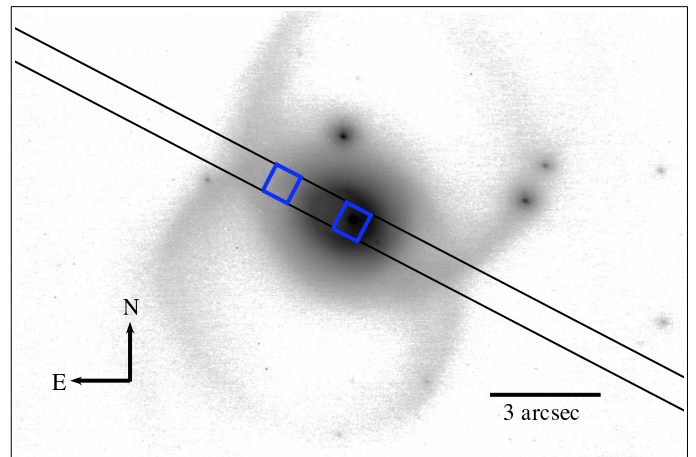
Fig. 4. Approximate ISAAC slit position displayed on NACO Ks image. Two boxes show the positions whose spectra have been displayed in Fig. 6.

between it and the corresponding broadband Ks image that the eye-shaped feature is dominated by H_2 line emission.

The bright central region of each image is reproduced in Fig. 2 at higher contrast to show the structure of the inner part of the nebula. Note that Figs. 1 and 2 are framed to progressively highlight the hourglass shape into the very central region of the eye. The broadband images again show a relatively smooth structure, dominated by an egg-shaped ring that is much brighter at its western, pointed end, just southwest of the central star. This ring was identified in the HST WFPC2 narrow-band optical images of Sahai et al. (1999) as ring 1. The central star is offset towards the narrow end of the ring, as noted by Sahai et al. (1999). An inner loop of emission corresponding to ring 2 is also apparent, particularly in the H_2 image.

Fig. 3 shows the central region of MyCn 18 in (a) H_2, identifying ring 1 and ring 2, and (b) in [N II]6584 Å, revealing the nebula's inner hourglass. Ring 1 is defined as the waist of the outer hourglass and ring 2 appears to be part of the inner hourglass, which is a higher excitation ring due to its close proximity with the central star (Sahai et al. 1999).

Fig. 3. Inner region of MyCn 18. (*a*) Image of ring 1 and ring 2 in H_2, and (*b*) the inner hourglass in HST [N II]6584 Å.

The images in both Figs. 1 & 2 have been reduced in the standard way, except that no flux calibration has been applied. Each image represents a reduced mean frame uncorrected for exposure time. The standard stars GSPC P550–C (RA=10h33m51.9s, Dec=+04d49m05.0s) and GSPC S889-E (RA=22h02m05.73s, Dec=−01d06m01.0s) were observed with the J, H, and Ks filters but we were unable to derive an accurate flux calibration, however, the results were broadly compatible with the overall calibrations found in Whitelock (1985).

The three continuum images in Fig. 1 all show faint relatively smooth emission from the edges of the main hourglass shell, together with a much brighter central region. The H_2 image in contrast shows a much clearer thin, filamentary eye-shaped feature surrounding the bright inner region. Although the H_2 image is not continuum subtracted, it is clear from the difference

2.2. Infra-red spectroscopy

Two-micron spectra of MyCn 18 were obtained with ISAAC (Moorwood et al. 1999) at the ESO Very Large Telescope (VLT) on 29 April 2004. An ISAAC short wavelength band was equipped with the Rockwell 1024 × 1024 array with pixel scale 0.145 arcsec in imaging mode and 0.147 arcsec in spectroscopic mode. The weather was clear, optical seeing varied between
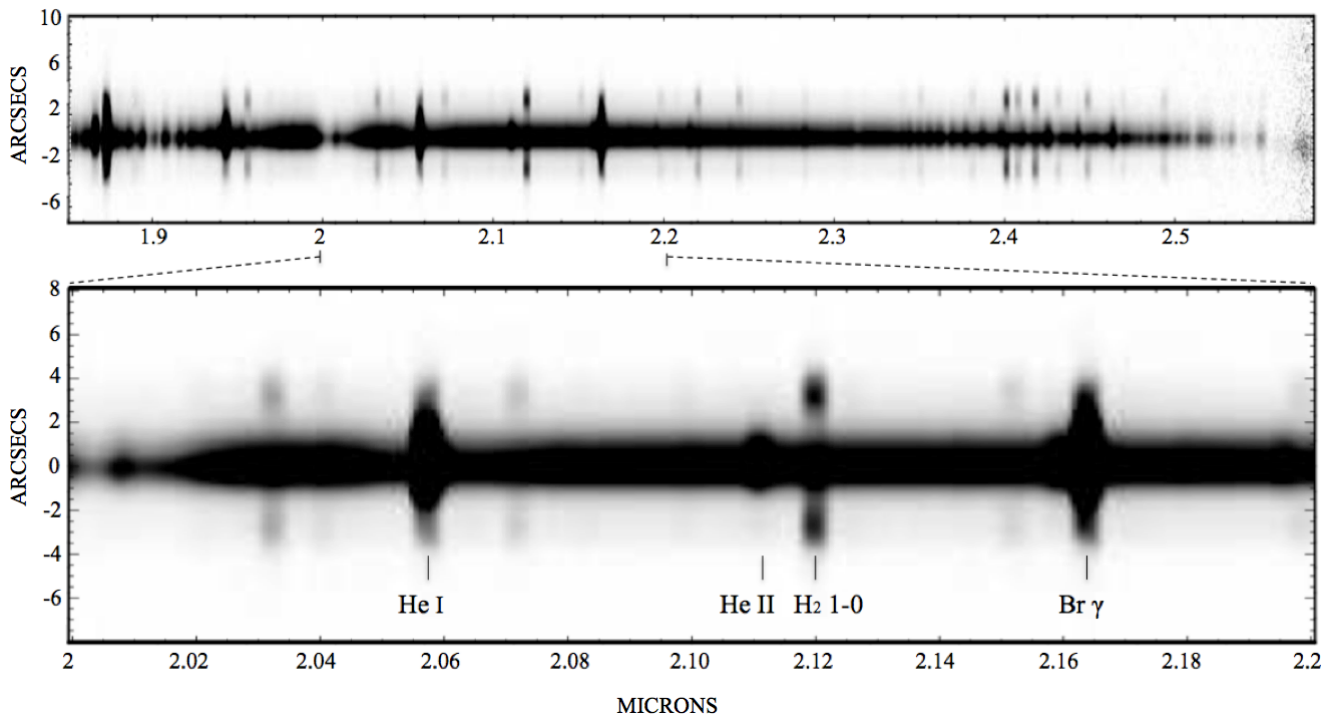
Fig. 5. A spatially resolved VLT ISAAC (outflow) spectrum. The spectrum, taken across the minor axis of the main hourglass shell, is shown at high contrast with the most prominent atomic and molecular emission lines visible. Two-micron spectrum (*top*), 2.25 arcsec from the central region along the nebula's minor axis, shows a plethora of strong He recombination and H_2 vibrational lines. Below is an enlarged view of the region of this spectrum over the range 2–2.2 micron. More details of this spectrum are shown in Fig. 6

0.92–1.37 arcsec and seeing at the K-band was approximately 0.75 arcsec during the acquisition of the target. The slit was placed along the minor axis of the nebula at a PA of 62.45° to the east (see Fig. 4) and the spatial scale was 0.15 arcsec per pixel. Low spectral resolution (LR) mode was used, and the slit width was 0.8 arcsec, resulting in a wavelength resolution ($R = \lambda/\Delta\lambda$) of 750. The telescope was nodded by 60 arcsec along the slit to cancel the sky background. Jitter was used along the slit to minimise the influence of hot pixels. An exposure of twilight sky was used for flat-fielding. The exposure time was 120 s × 16 on source.

The approximate ISAAC slit location is shown in Fig. 4 and the orientations of the slit are from northeast to southwest, which follow from top to bottom in the figure. The two boxes across the ISAAC slit represent the regions of the centre and outflow spectrum. The data were reduced using IDL and the ECLIPSE package. The telluric standard was the G2V star Hip 053690; Pickles (1998) calculated the spectrum of this star. The wavelength calibration is based on exposures of an Ar+Xe arc lamp with the same wavelength setting as the target observations. Additionally, OH skylines (Oliva & Origlia 1992; Maihara et al. 1993; Rousselot et al. 2000) and telluric absorption lines (Hadrava 2006) were used for the fine adjustment of the wavelength calibration.

The 2-D spectrum, shown at high contrast in Fig. 5, has been binned by 5 pixels along the slit length and indicates the most prominent atomic and molecular emission lines. The spectrum is seen to contain both continuum emission from the central region of MyCn 18 and line emission from the surrounding nebular shell. A spatially extended nebular continuum is clearly shown to be about 2 arcsec in extent and slightly offset with respect to the nebula's geometric centre. The continuum emission has a

faint extension to the east of the array. Two types of emission lines can be identified: one which is brightest in the core region and the other which is relatively faint in the core region but is brighter at each end, where the slit crosses the eastern and western edges of the nebula. This spectrum shows the spatial extent of H_2, He, and Br γ lines but is not corrected with telluric standard.

In Fig. 6, a K-band spectrum of MyCn 18 extracted from the central region is compared to a spectrum extracted from the nebular outflow region. The identifications of representative lines are also marked in the figure. In the central region, continuum is dominant, and both the central star and free-free and bound-free contribute to this continuum, as found in the images. This continuum contributes to approximately 8% of the total in-band flux in the Ks-band. There are strong H (Br γ and Br δ) and He recombination lines. Two H_2 lines can be identified at 1.95 μm 1–0 S(3) and 2.12 μm 1–0 S(1). The identifications of the lines beyond 2.35 μm are uncertain, but some H_2 lines are present. In contrast, a forest of H_2 lines is found in the outflow region, in addition to the H and He recombination lines.

The spectra shown in Fig. 5 and 6 demonstrate the spatial variations of the spectra across the object. The spectrum at the central region shows a strong underlying continuum across K-band spectra, particularly below the 2.2 μm wavelength. Strong H and He recombination lines are present in this region but H_2 lines are undetected. In contrast, the spectrum at the offset position, near the inner hourglass, is line dominated with some continuum. Here, He recombination lines are as strong as H recombination lines, but notably, much stronger H_2 lines are detected across this region. These spectra reveal the dominant contributors to the H_2 image (from Fig. 1) taken by the NACO. In the central region, there is a bright core found in the NB_2.122
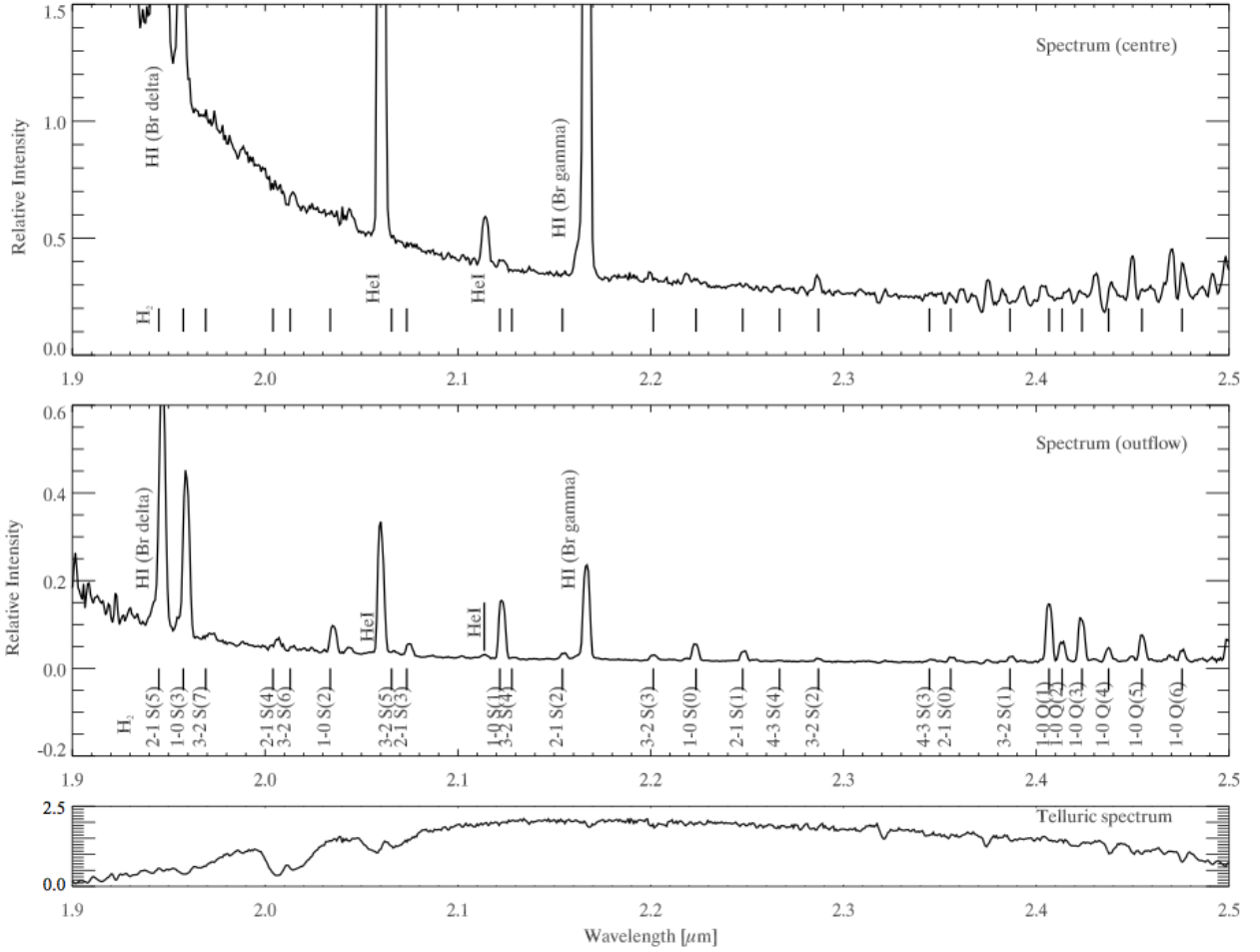
Fig. 6. Two-micron spectra of MyCn 18. Spectra for the central (*top*) 0.75 and offset (*middle*) 2.25 arcsec region are illustrated. Major H I and He II lines are indicated, and the expected positions of H_2 lines are marked. The bottom panel shows the atmospheric features.

image but this is due to continuum rather than H_2. This image shows clear bipolar shaped outflows, which outline the hourglass shape and this part is likely to be formed by H_2 emission lines. CO has a band of lines near/at the 2.3 μm line, which correspond to a large number of P- and R-branch vibrational-rotational transitions.

2.3. Optical Images & Spectroscopy

To aid our analysis of MyCn 18 we obtained optical images from the Hubble Legacy Archive[2] and ESO Archive, as well as MES and EMMI long-slit spectroscopic data.

Position-velocity (P-V) arrays of [N II]6584 Å line profiles from long-slit spectra were obtained along the major and minor axis of MyCn 18. These long-slit spectra were not flux calibrated and they have not been relatively calibrated either because we are primarily interested in the kinematics. Both sets of spectra are displayed with a linear scale.

The major nebula axis long-slit spectra were taken with the Anglo-Australian telescope (AAT) using the Manchester Echelle Spectrometer (MES; Meaburn et al. 1984) between 26 and 28

March 1999. A slit width of 150 μm, which is equivalent to 1 arcsec, was used and limits the resolution in the spectral direction to be 11 km s^{-1}. In the spatial direction, seeing was about 1 arcsec. The minor nebula axis long-slit spectra were obtained using ESO's Multi-Mode Instrument (EMMI; Dekker et al. 1986), which was attached to the ESO New Technology telescope (NTT), and spectra were taken on 23 March 1994. The seeing conditions are the same for those of the AAT, described above. For additional details on the MES and EMMI spectra, see O'Connor et al. (2000) and Corradi & Schwarz (1993), respectively.

3. Analysis

3.1. Infra-red images

The images were analysed, using IRAF[3], for possible companion stars to the nebula's primary. There is significant extinction and diffuse continuum emission to the centre of MyCn 18 (Bryce et al. 1997), which makes it difficult to resolve any close binary companions to the primary star. We believe the star located just SW of the central star in Fig. 3a has not been observed before.

---

[2] Based on observations made with the NASA/ESA Hubble Space Telescope, obtained from the data archive at the Space Telescope Institute. STScI is operated by the association of Universities for Research in Astronomy, Inc. under the NASA contract NAS 5-26555.

[3] IRAF is distributed by the National Optical Astronomy Observatories, which are operated by the Association of Universities for Research in Astronomy, Inc., under cooperative agreement with the National Science Foundation.
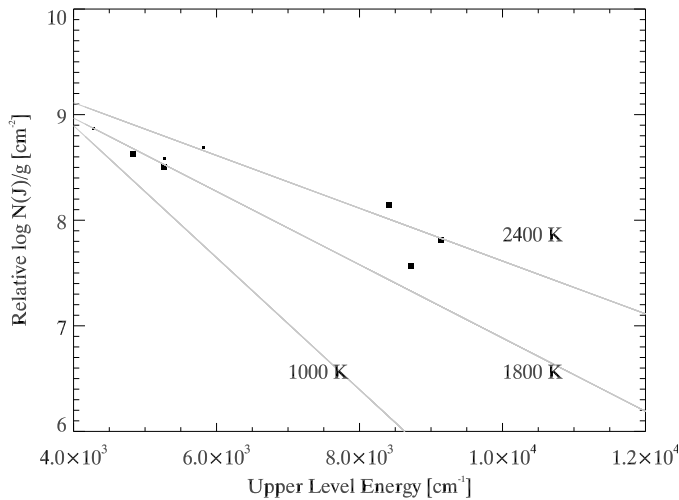
Fig. 7. An energy diagram of H_2 at 2.25 arcsec to the northeast of the central region. Squares show the measured line intensities and the lines show expected H_2 line intensities for a given temperature. The slopes of the lines indicate the temperature of the H_2 and shows the modelled energy distributions for 1000 K, 1800 K, and 2400 K, where the vertical scales are arbitrary. The H_2 excitation temperature is above 1800 K.

However, this star appears unlikely to be a candidate for association with the primary of MyCn 18 since it lies ~0.9 arcsec (~2,900 AU for a 3.2 kpc nebula distance) from the central star. Given that there are two other stars in the field of Fig. 3 then this newly observed star is also probably a field star; even if it were a companion, at this distance from the central star, it would have no direct dynamical effect on the shaping of the nebula.

Infrared contouring was later performed in and around the central region to search for even closer binary candidates. The astronomical data processing software STARLINK (Disney & Wallace 1982) and its KAPPA (Currie & Berry 2000) package were used to carry out the contouring. The reduced images in the H and Ks bands, as well as that in H_2, revealed some non-circular extension from the central star (see Fig. 3a). At first we thought this might be the result of a very close binary star, however, this non-point source appearance could be due to either (i) the aligning and co-adding of the images, (ii) poor psf as a result of adaptive optics, (iii) knotty emission from a recent ejection event or (iv) a line of sight star. Due to the large intensity of continuum surrounding the central star, it is not presently possible to distinguish further between these possibilities. Further high resolution observations of the central region would be required to reveal the nature of this source.

3.2. Spectroscopic analysis

There are prominent atomic recombination lines from the central region extending outwards beyond the main continuum band. The H_2 lines are clearly different in spatial extent and peak at about ±3 arcsec from the star. Comparing this spatial cut to the images, it can be seen that the H_2 emission comes from the cusps of the lenticular H_2 feature, which is most likely the line-of-sight overlap of the two lobes of the hourglass. Sahai et al. (1999) noted that the expected K-band flux (from the star) is about half the level observed by Whitelock (1985) and suggested this may indicate the presence of hot dust in the equatorial region. Our spectra show that this excess emission can be explained instead
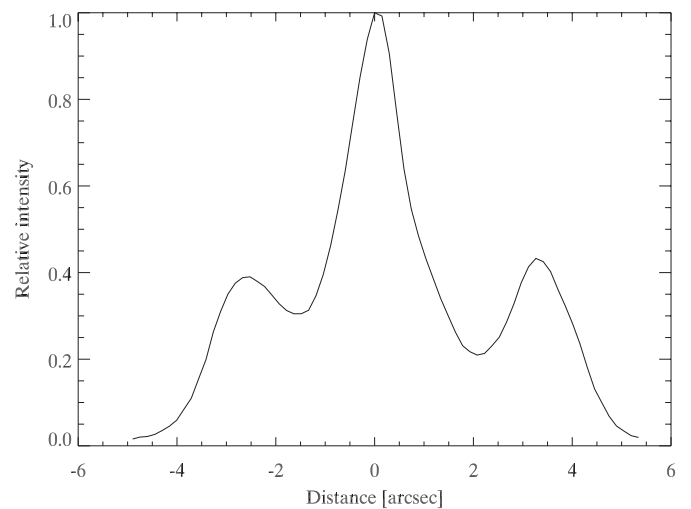

Fig. 8. A spatial cut through the H_2 1-0 S(1) line in Fig. 5 along the 2.122 micron pixel. The intensity distribution is shown and scaled at the peak.

by the strong free-free and atomic line emission from the compact ionised zone (Dayal et al. 1997; Koller & Kimeswenger 2000; Volk 2003; Ramos-Larios et al. 2012a). Silicates typically have a dust condensation temperature of ~1000 K, therefore, the peak of the dust emission would appear at a longer wavelength (2.9 μm) than what is observed in the spectra, which is actually < 1.9 μm. According to Corradi & Schwarz (1993), MyCn 18 peaks at about 60 μm (~48 K) and shows a typical double hump from its spectral energy distribution, indicating the presence of cool dust. Also, the light scattered by dust makes for an insignificant contribution to the nebula's central emission as noted by Sahai et al. (1999).

The resulting spectrum is the product of the nebula intensity gradient with a stratified ionisation structure, in which the least ionised layers are found furthest from the central star. The infrared spectroscopy shows clear ionisation stratification in that the He, H, and H_2 lines are found progressively further from the central star into the putative surrounding molecular torus. The nebula is likely to be ionisation bounded in the equatorial direction but since the high-speed knots are ionised the nebula is more likely to be density bounded in the polar direction (Dayal et al. 2000; Bains et al. 2002).

Fig. 7 shows the energy diagram of H_2 lines in the outflow. The slopes, derived from the H_2 lines, constrain the range of possible temperatures of the H_2 emitting gas under the LTE assumption. This gives a temperature range of 1800–2400 K, though higher excitation lines may deviate from LTE (Matsuura et al. 2007). The H_2 excitation temperature, estimated from rotation-vibrational lines, is as high as those estimated from similar lines of the Helix Nebula (1800 K; Matsuura et al. 2007) and the centre of NGC 6302 (1845 K; Davis et al. 2003) but much higher than temperatures estimated from rotation lines (below 1000 K; Cox et al. 1998; Bernard-Salas & Tielens 2005). It appears that rotation-vibrational temperatures are always higher near the central region of PNe. This might require an extra heating mechanism such as UV excitation (Henney et al. 2007) or shock excitation of H_2 (Burton et al. 1992).

The Ks band image in Fig. 2, which is dominated by the nebular continuum, shows an extent of about 2 arcsec across the central region. The spatial extent of the nebular continuum can also be readily seen in Fig. 5. Visually, it can be seen that the H_2
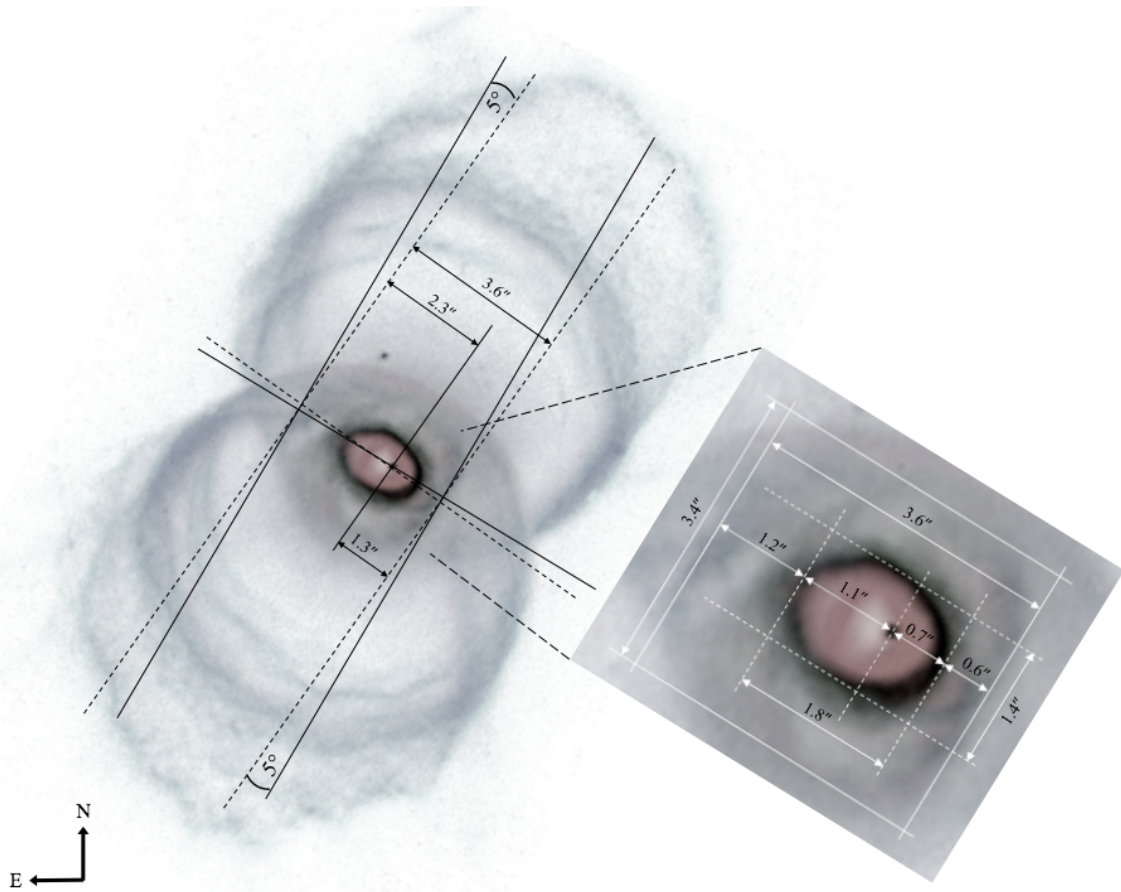
Fig. 9. An HST [N II]6584 Å image of MyCn 18. Shown is a geometric dimensional analysis of its inner and outer regions. The asymmetry of the nebula is obvious from the figure, with the inner hourglass being offset and slightly tilted ($\approx 5°$) with respect to the main hourglass shell and the central star is offset from the nebula's geometric centre.

1-0 line emission (at 2.12 μm) is found closer to the continuum in the negative spatial (SW) direction than the positive spatial (NE) direction, as shown in Fig. 8. This corresponds with the asymmetry seen in the continuum images of Fig. 2.

3.3. Geometric and timescale analysis of MyCn 18's nebular structures

The nebula has noticeable deviations from axial symmetry as illustrated in Fig. 9. The figure shows the relative offsets of the various features within the nebula. As shown, the central star is not centred on the nebula's major axis and is clearly offset along the minor axis. The star is also offset from the centre of ring 1 and is closer to the centre of ring 2 (see Fig. 3a). A close observation of the inner hourglass shows a slight tilt of its structure with respect to the outer hourglass. The image on the right of Fig. 9 shows the relative offsets of the inner hourglass, the nebular waist (ring 1), and the central star with respect to the nebula's geometric centre. In the case of the central star, it remains unclear as to why it is offset to the west of the nebular waist. An explanation of this offset may involve a binary companion.

In relation to MyCn 18's hypersonic knotty outflow, shown in Fig. 10, the paths taken by the knots are not symmetric about the axis of symmetry of the nebula's main hourglass (O'Connor et al. 2000). A closer inspection illustrates the scattering of the knots, with the northern cluster of knots found predominantly to the right of the main hourglass' axis of symmetry, and conversely, the southern cluster positioned to the left of this axis. The knots appear better aligned with the inner hourglass' axis of symmetry, thus supporting the hypothesis of a connection between these components.

The morphology and kinematics of MyCn 18 were better understood by applying timescales to each of its major components. These components include the main hourglass structure, the inner hourglass, and the high-speed interstellar knots. A distance of 2.4 kpc is routinely quoted for MyCn 18, which is inferred from a statistical method by Shklovsky (Schwarz et al. 1992). A more recent re-analysis of this method by Stanghellini et al. (2008) finds in particular that values derived in this way, by Corradi & Schwarz (1993), underestimate the distance for butterfly type planetary nebulae. They find a value for the distance to be 3.2 kpc. Other distances quoted in the literature range from 1 kpc to 3 kpc.

The fastest knots are travelling with speeds of ~500 km s^{-1} with the kinematical age of the fastest knot being ~1250 yrs (Bryce et al. 1997; O'Connor et al. 2000). Dayal et al. (2000) presented details of the velocities and corresponding timescales along different latitudes of the main hourglass and found the kinematical age of the nebula to be ~2500 yrs.

While the radius, R, of the nebula will vary linearly using the adopted distance, the expansion velocity follows a weaker power law in R ($V_{exp} \propto R^{(0.6\pm0.4)}$: Dayal et al. 2000), hence the nebula expansion timescale is less sensitive than the estimated timescale
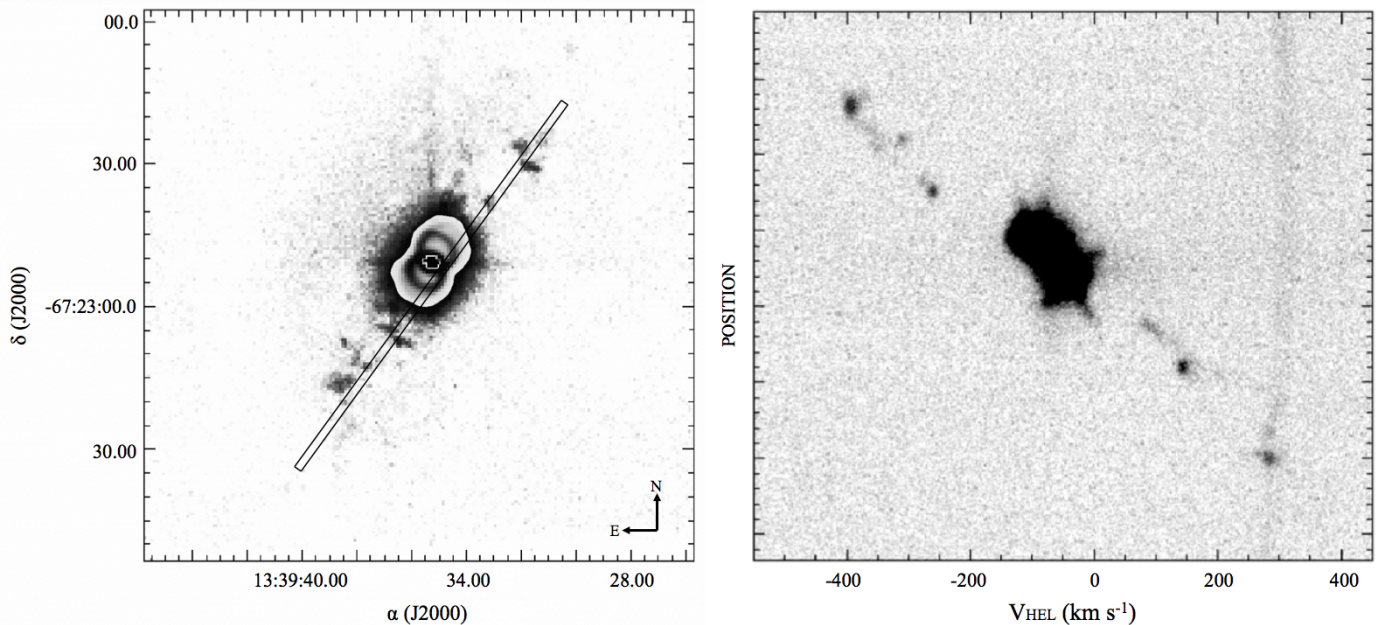
Fig. 10. Images of the hypersonic knotty outflow of MyCn 18. *Left*: a continuum subtracted image of MyCn 18 revealing the relative positions of the high-speed knots. *Right*: a P-V array for a long-slit placed down the nebula's major axis and through various knots, located north and south of the nebular lobes. The slit position shown on the left is a rough estimate of that used to produce the P-V array on the right. The knots south of the nebula (and through the slit) in the continuum subtracted image present the knots in the top left of the P-V array, and conversely, the knots north of the nebula present those in the bottom right. Both images in the figure are adopted from O'Connor et al. (2000).

of the ballistic ejection of the hypersonic knots. Our value for the kinematical age of the fastest knot, using the 3.2 kpc distance, is ~1650 yrs. With regards to the kinematical age of the nebula, the value obtained was ~2700 yrs.

The shape and structure of the inner hourglass appears similar to that of the main hourglass, which suggests that the mechanism that gave rise to the main hourglass might also be the same for that of the inner hourglass. Assuming this theory, the inner hourglass should follow a similar velocity law ($V_{exp} \propto R^{0.6\pm0.4}$) to that of the main hourglass. In this case, the expansion velocity of the inner hourglass would increase with increasing latitude along its walls, and is estimated to have an expansion velocity of 30 ± 5 km s^{-1} according to the synthetic P-V arrays generated from our SHAPE model. This corresponds to a timescale of 1750 ± 250 yrs. The interstellar knots have a similar kinematic age, thus implying that there might be a connection between them and the nebula's inner hourglass.

### 3.4. Morpho-kinematic modelling of MyCn 18: SHAPE analysis

While the hourglass morphology appears obvious, the significant inclination of MyCn 18 means that the structure and dynamics of the crucial region around the central star is not clear. Following the treatment of Hubble 12 in Vaytet et al (2009), the astrophysical modelling program SHAPE (version 4.51) was used to create the morpho-kinematics of MyCn 18 that were characterised by Bryce et al. (1997); Sahai et al. (1999); Dayal et al. (2000); O'Connor et al. (2000).

SHAPE is a software package that allows for the quick construction of many structures in 3-D and comparing these results with observed data assists in the interpretation of the object of interest. The geometry of each structure can be easily customised by means of a 3-D module and can be done either analytically or interactively. The application of a velocity field and

emission properties to such a 3-D structure model can allow for the generation of 2-D rendered images and P-V arrays, channel maps, light curves, and 1-D spectral line profiles (Steffen et al. 2011). Planetary nebulae such as NGC 2392 (García-Díaz et al. 2012), IC 418 (Ramos-Larios et al. 2012b), HaTr 4 (Tyndall et al. 2012), NGC 7026 (Clark et al. 2013) and Kn 26 (Guerrero et al. 2013) are all interesting examples that have recently been modelled using SHAPE.

A morpho-kinematic model of MyCn 18 was developed to allow for the reconstruction of its nebular morphology. Our aim, using SHAPE, involved creating a 3-D shape resembling the nebula using observed P-V arrays (optical long-slit spectra), which are compared and matched up with synthetic P-V arrays generated from our model.

Development of the model involved using three main structures; a cylinder (for the outer hourglass), a sphere (for the inner hourglass), and a torus (central 'eye' region). A cylinder, with a line type and a segment value of 30 (same in each structure), was used for the outer hourglass shell. A squeeze geometry modifier was then applied to the cylinder to give an hourglass shape with a tight waist of 1.8″. A velocity modifier, which is a velocity field as a function of position, was also applied to help determine the kinematics of the outer hourglass shell. The vector field of this velocity modifier was set to give a radial Hubble expansion of 0 km s^{-1} at the centre to 70 km s^{-1} at the poles using a radial power law. The velocity function is given by $|f|(r) = A + B(r/r_0) + C(r/r_0)^D$. The r (initial arbitrary radius assigned to the main hourglass structure) parameter is the only constant with a value of 100, whereas all other parameters are variables. The r_0 parameter is used to give the rate of change of velocity with respect to the radius r and has a value of 15. Parameters A and B are 0, whereas C and D are 2.2 and 1.82 respectively. Density modifiers, which set the spatial distribution of density, were used to give the arc-like etchings/rings on the outer hour-

9
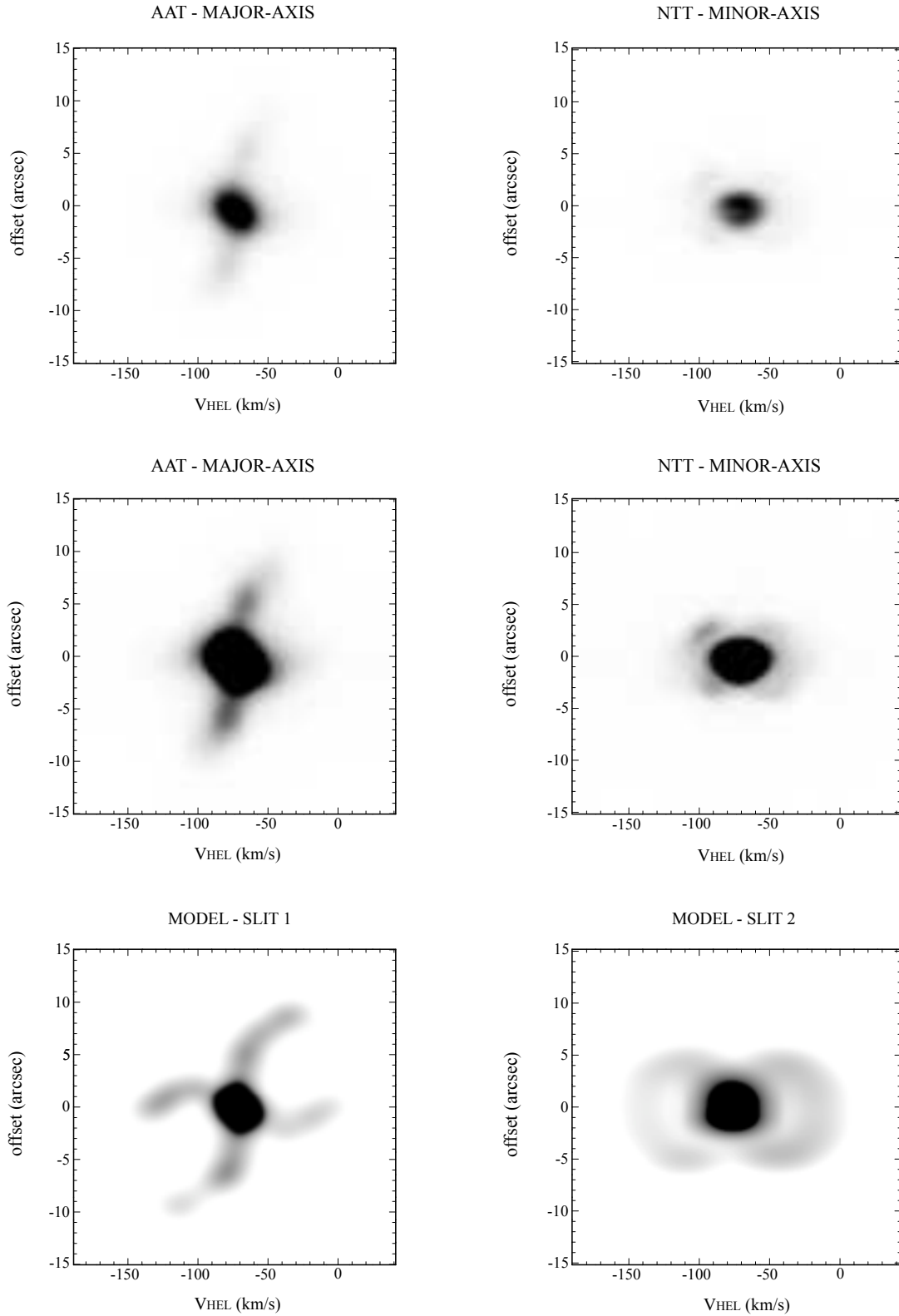
Fig. 11. MES, EMMI, and synthetic P-V arrays. The arrays on the left column (labelled AAT) are those for a long-slit applied to the major axis of the nebula using MES, whereas the right column (NTT) shows the arrays for a long-slit placed across the minor axis using EMMI (see Fig. 12b for these slit positions). The P-V arrays on the top panel and those on the central panel are the same, except using different stretches of the intensity scale. Shown at the bottom (MODEL) panel are the corresponding synthetic P-V arrays, which were generated using the SHAPE model.
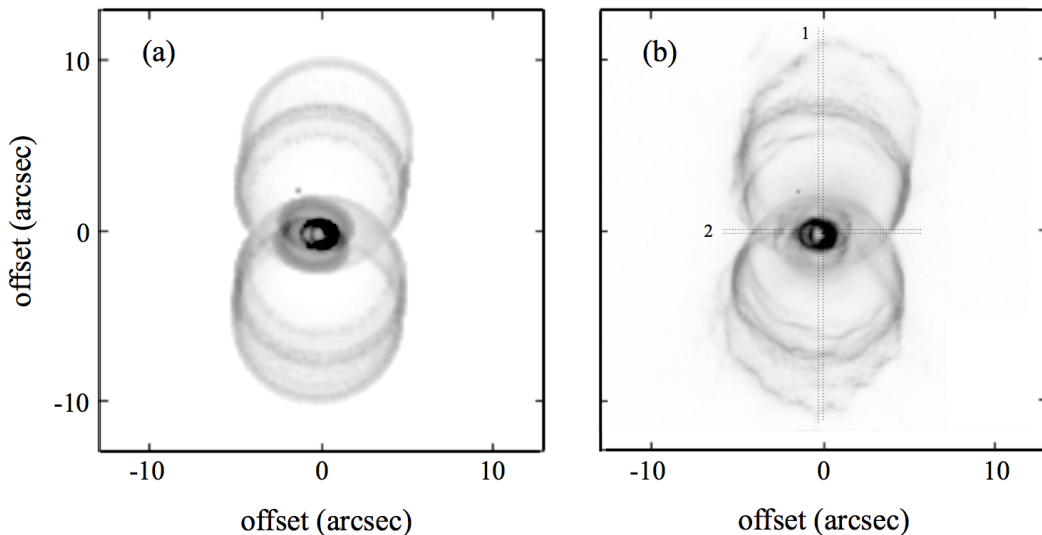
Fig. 12. The resultant SHAPE model of MyCn 18's nebular morphology and an HST[N II]6584 Å image scaled for comparison. Also shown are the long-slit positions used for the observed and synthetic P-V arrays in Fig. 11, labelled 1 (slit 1 down the major-axis) and 2 (slit 2 across the minor-axis). Both slit widths have a value of 0.8 arcsec.

glass shell. An arbitrary density scaling factor was used where the various structures were modified. A scaling factor of 1.0 was chosen for the main outer hourglass structure. The etchings/arcs, on each lobe, varied in density from 2.0 to 5.0. Two separate density modifiers were applied to the nebular waist (torus structure representing both ring 1 and ring 2). The first of these modifiers varied from 10 to 15 while the other (darkest region of the eye) varied from 15 to 20. All density values were chosen empirically by reference to the HST imagery of MyCn 18 from Sahai et al. (1999). Other modifiers such as shell thickness, size, and custom vertex were used to complete the outer hourglass structure. It should also be noted that the squeeze and density modifiers were set interactively, whereas the rest were set analytically. The inner hourglass was developed using a sphere. Again, a squeeze modifier was applied to give its hourglass shape, and a velocity modifier was set to give a radial expansion from 0 km s^{-1} at the centre to 30 km s^{-1} at the poles. The only different modifiers used for this structure were a translation modifier to allow for the offset (0.3″) of the structure and a rotation modifier to give the slight rotation (5°) of the inner hourglass with respect to the outer hourglass. The central eye region (nebular waist) of the nebula was constructed using a torus. The only modifiers not used for this structure were the squeeze, translation, and rotation modifiers. The expansion velocity is radially from 0 km s^{-1} at its centre to 10 km s^{-1} at its edge. A density modifier was used to give the ring 2 feature, as shown in Fig. 3a. The value for the inclination of each structure and their features is set to 38° on the 2-D rendering module, which corresponds to 90° − 38° = 52°. See Table 3 for the parameters used to create the model.

The P-V arrays shown in Fig. 11 (AAT & NTT arrays) and the associated P-V arrays from O'Connor et al. (2000) were used as the basis for the reconstruction process. Those observed spectra from Fig. 11 are shown at two different contrasts to display the spectroscopic features of MyCn 18. The stretches for the AAT spectra, from top to centre, are 0–60,000 and 0–15,000 counts respectively, and the stretches for the NTT spectra, from top to centre, are 0–40,000 and 0–10,000 counts, respectively. Also shown in Fig. 11 are synthetic P-V arrays, which were generated from the reconstructed model of MyCn 18 by means of a rendering module. The features of the synthetic P-V arrays re-

Table 3. The parameters for the best-fit SHAPE model of MyCn 18.

Parameter	Value
Pole-to-pole length (along its major axis)	18″
Nebular waist (along its minor axis)	1.8″
Max lobe width (along its minor axis)	8.5″
Shell thickness	0.2″
Inclination (w.r.t. plane of sky)	52°
Systemic heliocentric radial velocity, V_{sys}	−71 km s^{-1}
Max velocity (outer hourglass)	70 km s^{-1}
Max velocity (inner hourglass)	30 km s^{-1}
Convolution (seeing)	1.37″

Notes. The parameters for the velocity of the inner and outer hourglass varied until the observed and synthetic P-V arrays resembled each other closely. The slit width used in the modelling is the same as that used for the observed data.

veal more detail than those of the observed arrays because of the lesser seeing for the observed data on those given nights. It was for this reason that the P-V arrays from O'Connor et al. (2000) needed to be used also. The discrepancies in the observed data were brought out more clearly in the modelled arrays by varying the convolution (seeing) parameters on the rendering module of SHAPE. Figs. 11 and 12 were colour-inverted and grey-scaled for clear presentation.

A systemic heliocentric velocity, V_{sys}, of −71 km s^{-1} (O'Connor et al. 2000) was used as the central velocity in the synthetic P-V arrays. The brightness of the observed P-V arrays varies from low to high for a long-slit placed directly down the major axis of the nebula and across its minor axis. The MES arrays (major-axis arrays) show the lobed features, which are more visible in the higher brightness image. The same features are clearly displayed in the model slit 1 synthetic array with better seeing than the observed MES arrays. It is apparent that both the observed and synthetic arrays follow a similar pattern, which

11

closely indicates that the shape of MyCn 18 is an open ended, bilobed, bipolar nebula.

The rates of expansion (in km s^{-1}) from the geometric centre out to the end of each lobe and across the waist were determined from the synthetic arrays. Having applied the appropriate velocity components, using the SHAPE velocity modifiers, the velocity scale can be centred at $V_{\mathrm{HEL}} = -71$ km s^{-1}, the velocity defined with respect to the nebula's frame of reference in which the Sun is at rest. Two distinctly separate velocity features are present in the model slit-1 and MES arrays with the first around 0″ offset from $V_{\mathrm{HEL}} = 0$ to -140 km s^{-1} and the other from $V_{\mathrm{HEL}} = -30$ to -120 km s^{-1} for the model slit-1 array. The MES arrays, however, do not show emission out to these velocities, therefore, the P-V arrays from O'Connor et al. (2000) [see Fig. 3] were used to help finalise the synthetic arrays. These velocities obtained closely resemble those found by O'Connor et al. (2000) for their observed data.

The finished model, shown in Fig. 12a as a 2-D rendered image, has the same inclination (with the top, southeastern, half of the hourglass tilted towards us at an angle of 52° with respect to the plane of the sky) and is closely scaled to that shown in Fig. 12b, which is an HST [N II]6584 Å image for comparison. It should also be noted that the seeing used for the 2-D rendered image is 0.3 arcsec instead of the 1.37 arcsec used when generating the synthetic P-V arrays, and the structures of the observed P-V arrays are smeared due to the 1.37 arcsec seeing, which makes it difficult to get a precise measurement of the expansion.

4. Discussion

4.1. Shaping mechanisms and offsets

Although there is still much to be understood about the complexity of MyCn 18's asymmetry, we here propose explanations as to why this might be. Currently, the binary scenario is the favoured mechanism for the creation of bipolar planetary nebulae (Morris 1987; Han et al. 1995; Soker & Rappaport 2000; Balick & Frank 2002; De Marco 2009; Jones et al. 2010; Soker & Kashi 2012). Companion stars may likely exist within the central eye region of MyCn 18, however, since they cannot be observed directly, their luminosity must be low in comparison to the neighbouring central star, and any continuum surrounding the central region would certainly obscure their light.

In relation to the offset of the central star, one proposed theory involves a variable accretion of matter onto the central white dwarf, resulting in a dwarf nova explosion that could have kicked the star off in one direction while producing the disrupted region of the eye in the opposite direction (see N-E region of ring 1 in Fig. 3b). Assuming momentum conservation of the ejecta+star system before and after the explosion, we determine an energy of 7.2 x 10^{43} ergs for a velocity of 600 km s^{-1} (Bryce et al. 1997; O'Connor et al. 2000) and a mass of 10^{-5} M$_\odot$ (Sahai et al. 1999) for the knotty ejecta. From Fig. 9, we see that the star is offset from ring 1 by 0.2″, which corresponds to 640 AU for a distance of 3.2 kpc, and the time taken for the star to move from the nebula's geometric centre to its current position is 1050 yrs (the difference between the age of the nebula and the knotty ejecta: 2700−1650 yrs). Using these values, we find that the star would have to be moving at a velocity of ∼3 km s^{-1} over that period. For a 0.6 M$_\odot$ white dwarf and a velocity of 3 km s^{-1}, we find an energy of 5.4 x 10^{43} ergs, which closely resembles that of the energy for the ejecta plus star system.

The nebula's other prominent features are also offset with respect to the geometric centre. The offset, and even the creation, of the inner hourglass may be the result of the formation of the knots since its axis of symmetry appears to follow the path taken by the knots. Our calculation for the kinematical age of the inner hourglass corresponds closely to that of the knots, which further suggests a possible connection between both components.

The younger, high-speed knots might explain the truncated, open-ended lobes of the outer hourglass. At an earlier epoch, before the creation of the knots, the ends of the lobes may have been closed. Some time after, the high-speed ejection of the knots would have penetrated the lobed ends, giving rise to their truncation, thus suggesting the younger age of the knots. This penetration would have occurred when the outer hourglass was smaller than it is now, which could explain for the large opening angle of each lobe (see Sahai & Trauger 1998).

Soker & Kashi (2012) propose that the formation of bipolar lobes of some PNe and pre-PNe are the result of one or more intermediate-luminosity optical transient (ILOT) events. Jets created by the accretion of matter, from an AGB (or extreme-AGB) star, onto a main-sequence companion are launched by an accretion disk, which in turn shapes the bipolar lobes. For MyCn 18 to form from an ILOT event, it would need to have a linear velocity-distance relation, a bipolar structure, an expansion velocity (for the knotty outflow) of ∼100–1000 km s^{-1}, and a total kinetic energy of ∼10^{46}–10^{49} ergs, as noted by Soker & Kashi (2012). They show that MyCn 18 has all the characteristic properties of an ILOT event apart from the total kinetic energy, which is of the order ∼10^{44} ergs, and their energy-time diagram (ETD) shows MyCn 18 to be just outside the optical transient stripe (OTS), making it an exception. MyCn 18 does not appear energetic enough to be a ILOT event. They support the O'Connor et al. (2000) view that MyCn 18 was formed by a nova like explosion instead. However, in the light of the recent frequent discovery of hot Jupiter-type planets, it is possible to generate an ILOT event of significantly lower energy than envisaged by Soker & Kashi (2012). A planet engulfed at the AGB phase, surviving to spiral through the tenuous envelope to the dense core of the star and finally forming an accretion disk there (Nordhaus & Blackman 2006), gives a natural mechanism for breaking the spherical symmetry of the AGB phase. Subsequently a nova-type explosion event on the degenerate core could have led to the generation of the hypersonic knots and the deviations from cylindrical symmetry of the nebula and the offset location of its central star.

A planet destruction event causing an asymmetric nova explosion could explain features as follows: on the AGB phase, a planet is engulfed and survives long enough to disrupt the symmetry of the nebula and cause its bipolar shape. As the planet spirals to the degenerate core an accretion disk forms and we speculate that the final accretion event of the planet onto the star generates an explosion that is localised on the stellar core. This asymmetric explosion gives a velocity kick to the star, generates the knotty outflow perpendicular to the disk, and causes the disruption to ring 1 in the opposite (NE) direction to the star's movement (this is observed better in the composite colour image from Sahai et al. 1999).

Interestingly, despite the expectation that planets should be readily detectable around white dwarfs (Burleigh et al. 2001) they have not been observed yet (Mustill & Villaver 2012), which may suggest that many hot Jupiter exoplanets are readily engulfed and destroyed at the AGB phase. Since there are not enough close binaries to shape the large fraction of non-spherical

PNe, this strongly suggests some role for planets in their shaping (De Marco & Soker 2011).

4.2. Morpho-kinematic modelling

Our long-slit spectra provided us with sufficient information about the 3-D structure of the nebula, which allowed us to generate a self-consistent 3-D model. Density distributions and velocity parameters were applied to the individual sub-systems in order to generate the synthetic P-V arrays needed for describing the kinematics of the nebula. This technique, along with the long-slit spectra, enabled us to reconstruct the shape of the nebula. The resultant 3-D SHAPE model is in good agreement with that of Sahai et al. (1999); Dayal et al. (2000), specifically for the structure and kinematics of this gaseous nebula.

It has been shown, by use of the observed and synthetic P-V arrays, that the expansion rate of the nebula follows that of a Hubble-type expansion, i.e., the velocity of the ionised gas increases linearly with distance from the centre (Solf & Ulrich 1985; Icke et al. 1989). Our values for the expansion rates correspond closely to those found by O'Connor et al. (2000). The kinematical age of MyCn 18 was then found to be ~2700 yrs using these velocities. Although a distance of 3.2 kpc was used to help determine an age for MyCn 18, it is still not accepted as a confirmed distance, therefore, other techniques are required to narrow down the possible range.

An unambiguous distance measurement requires a proper motion study of the high velocity knots of MyCn 18 or hourglass edges. The proper motion for a given feature is $0.02 \, V_{100}/D_{\text{kpc}}$ arcsec yr^{-1}, where V_{100} is the velocity in units of 100 km s^{-1} and D_{kpc} is the distance in units of kpc. The original HST images of MyCn 18 were taken in the mid 1990s so displacement of the 500 km s^{-1} knots should be detectable in a second epoch image even if the distance to MyCn 18 is up to 3.2 kpc. The second epoch which included the NTT EFOSC frames were analysed to determine the relative positions of the knots. Unfortunately, the exposure times were much too short to reveal any knots that might have moved.

5. Conclusions

We have carried out an optical and infrared study of MyCn 18 in order to understand the whole structure and dynamics of the nebula from the offset central star to the striking nebula morphology and the distant hypersonic knotty outflow. VLT IR observations of MyCn 18 were combined with earlier optical work, morpho-kinematic modelling, and a search for a close stellar binary companion. We consider that the conventional planetary nebula formation process has been significantly affected by an explosive event that has led to deviations from axial symmetry such as a displacement of the central star and the misalignment of the main nebular structures. We speculate that a hot Jupiter exoplanet was engulfed at the AGB phase of the star's evolution and that the accretion of this material onto the core of the star led to a nova-type explosion that was ultimately responsible for the hypersonic knotty outflow. Given the common nature of hot Jupiters, it can even be suggested that this and other extreme bipolar morphology planetary nebulae are ultimately shaped by one or more exoplanets.

References

Aleman, I. & Gruenwald, R. 2004, ApJ, 607, 865
Bains, I., Bryce, M., Calabretta, M., & Stirling, A. M. 2002, MNRAS, 337, 401
Balick, B. 1987, AJ, 94, 671
Balick, B. & Frank, A. 2002, ARA&A, 40, 439
Bernard-Salas, J. & Tielens, A. G. G. M. 2005, A&A, 431, 523
Bryce, M., Lopez, J. A., Holloway, A. J., & Meaburn, J. 1997, ApJ, 487, L161+
Burleigh, M., Clarke, F., & Hodgkin, S. 2001, in Techniques for the Detection of Planets and Life beyond the Solar System, ed. W. R. F. Dent, 15
Burton, M. G., Hollenbach, D. J., & Tielens, A. G. G. 1992, ApJ, 399, 563
Cavanagh, B., Jenness, T., Economou, F., & Currie, M. J. 2008, Astronomische Nachrichten, 329, 295
Chevalier, R. A. & Luo, D. 1994, ApJ, 421, 225
Clark, D. M., López, J. A., Steffen, W., & Richer, M. G. 2013, AJ, 145, 57
Corradi, R. L. M. & Schwarz, H. E. 1993, A&A, 268, 714
Cox, P., Boulanger, F., Huggins, P. J., et al. 1998, ApJ, 495, L23+
Currie, M. J. & Berry, D. S. 2000, Starlink User Note 95
Currie, M. J. & Cavanagh, B. 2004, ORAC-DR - imaging data reduction, starlink User Note 232.8
Davis, C. J., Smith, M. D., Stern, L., Kerr, T. H., & Chiar, J. E. 2003, MNRAS, 344, 262
Dayal, A., Sahai, R., Trauger, J., et al. 1997, in Bulletin of the American Astronomical Society, Vol. 29, American Astronomical Society Meeting Abstracts, 1234
Dayal, A., Sahai, R., Watson, A. M., et al. 2000, AJ, 119, 315
De Marco, O. 2009, PASP, 121, 316
De Marco, O. & Soker, N. 2011, PASP, 123, 402
Dekker, H., Delabre, B., & Dodorico, S. 1986, in Society of Photo-Optical Instrumentation Engineers (SPIE) Conference Series, Vol. 627, Society of Photo-Optical Instrumentation Engineers (SPIE) Conference Series, ed. D. L. Crawford, 339–348
Disney, M. J. & Wallace, P. T. 1982, QJRAS, 23, 485
Douchin, D., De, M. O., Jacoby, G. H., et al. 2012, in SF2A-2012: Proceedings of the Annual meeting of the French Society of Astronomy and Astrophysics, ed. S. Boissier, P. de Laverny, N. Nardetto, R. Samadi, D. Valls-Gabaud, & H. Wozniak, 325–327
Eyermann, S. E. & Speck, A. K. 2004, in Bulletin of the American Astronomical Society, Vol. 36, American Astronomical Society Meeting Abstracts, 138.11
García-Díaz, M. T., López, J. A., Steffen, W., & Richer, M. G. 2012, ApJ, 761, 172
García-Segura, G., Langer, N., Różyczka, M., & Franco, J. 1999, ApJ, 517, 767
Guerrero, M. A., Miranda, L. F., Ramos-Larios, G., & Vázquez, R. 2013, A&A, 551, A53
Hadrava, P. 2006, A&A, 448, 1149
Han, Z., Podsiadlowski, P., & Eggleton, P. P. 1995, MNRAS, 272, 800
Henney, W. J., Williams, R. J. R., Ferland, G. J., Shaw, G., & O'Dell, C. R. 2007, ApJ, 671, L137
Hora, J. L. & Latter, W. B. 1996, in Bulletin of the American Astronomical Society, Vol. 28, American Astronomical Society Meeting Abstracts, 1402
Hora, J. L., Latter, W. B., Marengo, M., et al. 2005, in Bulletin of the American Astronomical Society, Vol. 37, American Astronomical Society Meeting Abstracts #206, 493
Icke, V., Preston, H. L., & Balick, B. 1989, AJ, 97, 462
Jones, D., Lloyd, M., Santander-García, M., et al. 2010, MNRAS, 408, 2312
Jones, D., Mitchell, D. L., Lloyd, M., et al. 2012, MNRAS, 420, 2271
Jordan, S., Bagnulo, S., Werner, K., & O'Toole, S. J. 2012, A&A, 542, A64
Kastner, J. H., Gatley, I., & Weintraub, D. A. 2000, in Astronomical Society of the Pacific Conference Series, Vol. 199, Asymmetrical Planetary Nebulae II: From Origins to Microstructures, ed. J. H. Kastner, N. Soker, & S. Rappaport, 355
Kastner, J. H., Henn, L., Weintraub, D. A., Gatley, I., & Siebenmorgen, R. 1998, in Bulletin of the American Astronomical Society, Vol. 30, American Astronomical Society Meeting Abstracts, 1274
Koller, J. & Kimeswenger, S. 2000, Thermal Emission Spectroscopy and Analysis of Dust, Disks, and Regoliths, 196, 23
Kwok, S. 1982, ApJ, 258, 280

Kwok, S., Purton, C. R., & Fitzgerald, P. M. 1978, ApJ, 219, L125

Lee, T.-H., Stanghellini, L., Ferrario, L., & Wickramasinghe, D. T. 2007, in Astronomical Society of the Pacific Conference Series, Vol. 372, 15th European Workshop on White Dwarfs, ed. R. Napiwotzki & M. R. Burleigh, 173

Lenzen, R., Hartung, M., Brandner, W., et al. 2003, in Society of Photo-Optical Instrumentation Engineers (SPIE) Conference Series, Vol. 4841, Society of Photo-Optical Instrumentation Engineers (SPIE) Conference Series, ed. M. Iye & A. F. M. Moorwood, 944–952

Likkel, L., Kindt, A., Dinerstein, H. L., & Lester, D. F. 2000, in Astronomical Society of the Pacific Conference Series, Vol. 199, Asymmetrical Planetary Nebulae II: From Origins to Microstructures, ed. J. H. Kastner, N. Soker, & S. Rappaport, 333

Maihara, T., Iwamuro, F., Yamashita, T., et al. 1993, PASP, 105, 940

Matsuura, M., Speck, A. K., Smith, M. D., et al. 2007, MNRAS, 382, 1447

Matsuura, M. & Zijlstra, A. 2005, in High Resolution Infrared Spectroscopy in Astronomy, ed. H. U. Käufl, R. Siebenmorgen, & A. Moorwood, 423–426

Meaburn, J., Blundell, B., Carling, R., et al. 1984, MNRAS, 210, 463

Moorwood, A., Cuby, J.-G., Ballester, P., et al. 1999, The Messenger, 95, 1

Morris, M. 1987, PASP, 99, 1115

Mustill, A. J. & Villaver, E. 2012, ApJ, 761, 121

Nordhaus, J. & Blackman, E. G. 2006, MNRAS, 370, 2004

O'Connor, J. A., Redman, M. P., Holloway, A. J., et al. 2000, ApJ, 531, 336

Oliva, E. & Origlia, L. 1992, A&A, 254, 466

Pascoli, G. & Lahoche, L. 2008, PASP, 120, 1267

Pickles, A. J. 1998, PASP, 110, 863

Ramos-Larios, G., Guerrero, M. A., & Miranda, L. F. 2008, AJ, 135, 1441

Ramos-Larios, G., Guerrero, M. A., Suárez, O., Miranda, L. F., & Gómez, J. F. 2012a, A&A, 545, A20

Ramos-Larios, G., Vázquez, R., Guerrero, M. A., et al. 2012b, MNRAS, 423, 3753

Rousselot, P., Lidman, C., Cuby, J.-G., Moreels, G., & Monnet, G. 2000, A&A, 354, 1134

Rousset, G., Lacombe, F., Puget, P., et al. 2003, in Society of Photo-Optical Instrumentation Engineers (SPIE) Conference Series, Vol. 4839, Society of Photo-Optical Instrumentation Engineers (SPIE) Conference Series, ed. P. L. Wizinowich & D. Bonaccini, 140–149

Sahai, R., Dayal, A., Watson, A. M., et al. 1999, AJ, 118, 468

Sahai, R., Sugerman, B. E. K., & Hinkle, K. 2009, ApJ, 699, 1015

Sahai, R. & Trauger, J. T. 1998, AJ, 116, 1357

Schwarz, H. E., Corradi, R. L. M., & Melnick, J. 1992, A&AS, 96, 23

Sellgren, K., Bromm, V., & Dinerstein, H. 2008, Spitzer Proposal, 50179

Soker, N. & Harpaz, A. 1992, PASP, 104, 923

Soker, N. & Kashi, A. 2012, ApJ, 746, 100

Soker, N. & Rappaport, S. 2000, ApJ, 538, 241

Soker, N. & Rappaport, S. 2001, ApJ, 557, 256

Solf, J. & Ulrich, H. 1985, A&A, 148, 274

Stanghellini, L., Shaw, R. A., & Villaver, E. 2008, ApJ, 689, 194

Steffen, W., Koning, N., Wenger, S., Morisset, C., & Magnor, M. 2011, IEEE Transactions on Visualization and Computer Graphics, 17, 454

Tenenbaum, E. D., Milam, S. N., Woolf, N. J., & Ziurys, L. M. 2009, ApJ, 704, L108

Trammell, S. R., Dinerstein, H. L., & Goodrich, R. W. 1995, in Annals of the Israel Physical Society, Vol. 11, Asymmetrical Planetary Nebulae, ed. A. Harpaz & N. Soker, 37

Tyndall, A. A., Jones, D., Lloyd, M., O'Brien, T. J., & Pollacco, D. 2012, MNRAS, 422, 1804

Vlemmings, W. 2012, in IAU Symposium, Vol. 283, IAU Symposium, 176–179

Vlemmings, W. H. T. 2011, in Asymmetric Planetary Nebulae 5 Conference

Volk, K. 2003, in IAU Symposium, Vol. 209, Planetary Nebulae: Their Evolution and Role in the Universe, ed. S. Kwok, M. Dopita, & R. Sutherland, 281

Wang, M.-Y., Muthumariappan, C., & Kwok, S. 2006, in IAU Symposium, Vol. 234, Planetary Nebulae in our Galaxy and Beyond, ed. M. J. Barlow & R. H. Méndez, 537–538

Whitelock, P. A. 1985, MNRAS, 213, 59

Yungelson, L. R., Tutukov, A. V., & Livio, M. 1993, ApJ, 418, 794
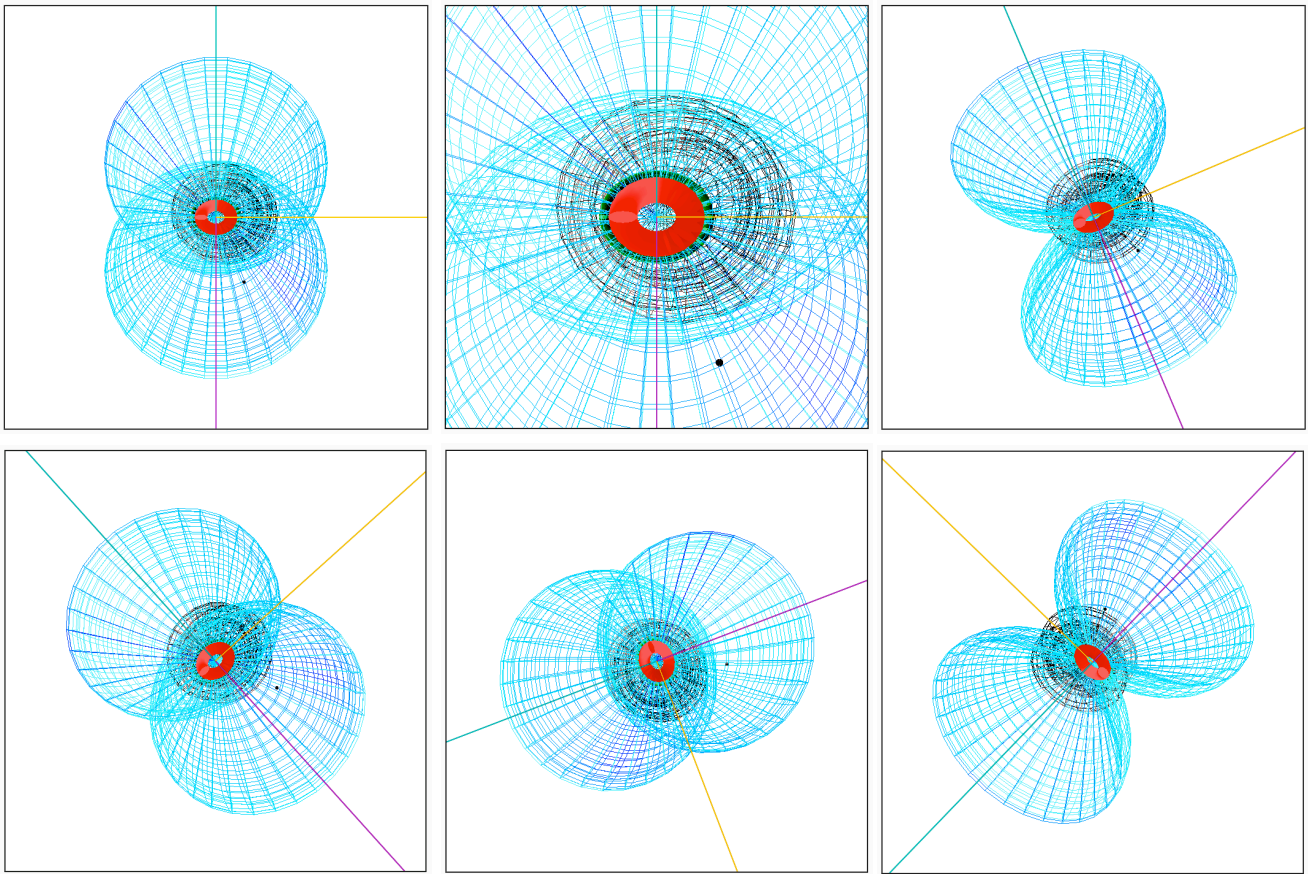
Fig. .1. SHAPE model of MyCn 18 from different points of view.

Appendix A: SHAPE **images of MyCn 18**

Shown above is the SHAPE model for MyCn 18 from different viewing angles. The green, yellow, and purple line represent the top view, right view, and axis of symmetry of the nebula, respectively. The top left view shows the nebula with its southern pole tilted towards us at an angle of 52° with respect to the plane of the sky. From top to bottom on this view represents a NW to SE direction. The view on the top middle is a close in of the first showing detail of the inner part of the nebula.